

IEEE TRANSACTIONS ON GEOSCIENCE AND REMOTE SENSING

A PUBLICATION OF THE IEEE GEOSCIENCE AND REMOTE SENSING SOCIETY



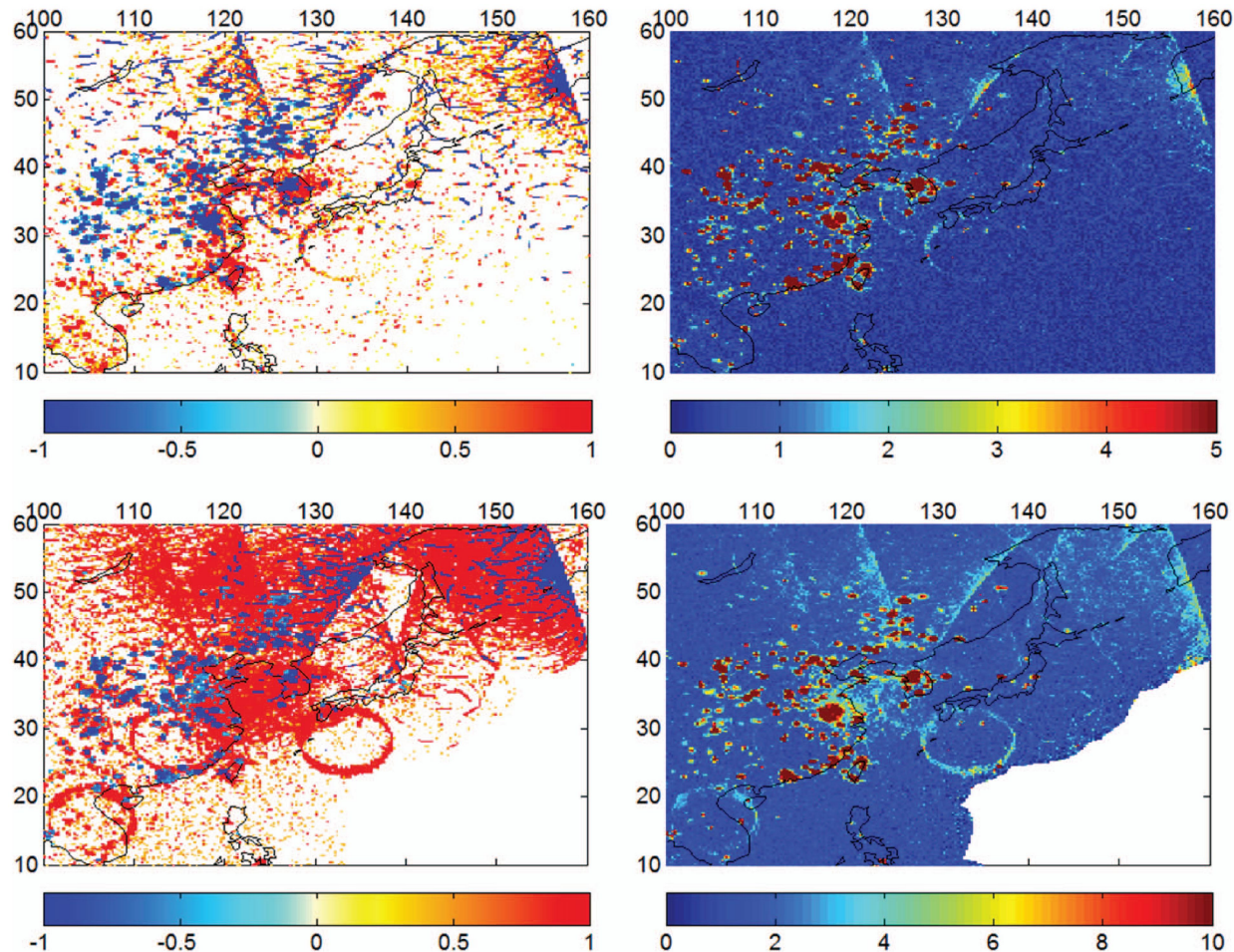
OCTOBER 2016

VOLUME 54

NUMBER 10

IGRSD2

(ISSN 0196-2892)



Excess kurtosis values and associated RFI detection rates in East Asia and Japan, as measured by the SMAP mission 1400–1427 MHz radiometer for the period June 3, 2015 to June 9, 2015. The top two figures are excess kurtosis values (left) and kurtosis detection rate (right) over East Asia derived from the full-bandwidth data stream. The bottom two show similar information obtained from the channelized data stream.

IEEE TRANSACTIONS ON GEOSCIENCE AND REMOTE SENSING

A PUBLICATION OF THE IEEE GEOSCIENCE AND REMOTE SENSING SOCIETY



OCTOBER 2016

VOLUME 54

NUMBER 10

IGRSD2

(ISSN 0196-2892)

PAPERS

Atmosphere

- Water Vapor Pressure Model for Cloud Vertical Structure Detection in Tropical Region
F. Yuan, Y. H. Lee, Y. S. Meng, and J. T. Ong 5875

Vegetation and Land

- Large-Scale Biomass Classification in Boreal Forests With TanDEM-X Data
A. Toraño Caicoya, F. Kugler, I. Hajnsek, and K. P. Papathanassiou 5935

Electromagnetics

- A Frequency-Hopping Subspace-Based Optimization Method for Reconstruction of 2-D Large Uniaxial Anisotropic Scatterers With TE Illumination Y. Liu, Z. Zhao, Y. Yang, B. Wang, X. Zhu, Z. Nie, and Q. H. Liu 6091

Hyperspectral Data Processing

- A Deterministic Method for Profile Retrievals From Hyperspectral Satellite Measurements
P. K. Koner, A. R. Harris, and P. Dash 5657

- A Computationally Efficient Algorithm for Fusing Multispectral and Hyperspectral Images
R. Guerra, S. López, and R. Sarmiento 5712

- A Tensor Decomposition-Based Anomaly Detection Algorithm for Hyperspectral Image
X. Zhang, G. Wen, and W. Dai 5801

- Spectral Unmixing Using a Sparse Multiple-Endmember Spectral Mixture Model
F. Chen, K. Wang, and T. F. Tang 5846

- Hyperspectral Image Compression Optimized for Spectral Unmixing A. Karami, R. Heylen, and P. Scheunders
Iterative Curve Fitting: A Robust Technique to Estimate the Wavelength Position and Depth of Absorption Features
From Spectral Data S. Asadzadeh and C. R. de Souza Filho 5964

- Robust Collaborative Nonnegative Matrix Factorization for Hyperspectral Unmixing
J. Li, J. M. Bioucas-Dias, A. Plaza, and L. Liu 6076

- Statistical Volume Analysis: A New Endmember Extraction Method for Multi/Hyperspectral Imagery
X. Geng, L. Ji, F. Wang, Y. Zhao, and P. Gong 6100

- Multidomain Subspace Classification for Hyperspectral Images L. Zhang, X. Zhu, L. Zhang, and B. Du 6138

(Contents Continued on Page 5630)

Semisupervised Sparse Manifold Discriminative Analysis for Feature Extraction of Hyperspectral Images	6197
Deep Feature Extraction and Classification of Hyperspectral Images Based on Convolutional Neural Networks	6232
Image Processing and Analysis	
Extinction Profiles for the Classification of Remote Sensing Data	5631
A Robust Method to Generate a Consistent Time Series From DMSP/OLS Nighttime Light Data	5821
Ship Detection in Spaceborne Optical Image With SVD Networks	5832
Development of a Large-Format UAS Imaging System With the Construction of a One Sensor Geometry From a Multicamera Array	5925
Object-Based Morphological Profiles for Classification of Remote Sensing Imagery	5952
A Three-Layered Graph-Based Learning Approach for Remote Sensing Image Retrieval	6020
Multiscale and Multifeature Normalized Cut Segmentation for High Spatial Resolution Remote Sensing Imagery	6061
Microwave Radiometry	
SMAP L-Band Microwave Radiometer: RFI Mitigation Prelaunch Analysis and First Year On-Orbit Observations	6035
Radar Systems	
Radar Sounding Using the Cassini Altimeter: Waveform Modeling and Monte Carlo Approach for Data Inversion of Observations of Titan's Seas	5646
Adaptive Beamspace Processing for Phased-Array Weather Radars	5688
Analysis and Validation of High-Resolution Wind From ASCAT	5699
A Technique to Improve Copolar Correlation Coefficient Estimation	5776
Airborne Co-polarization and Cross-Polarization Observations of the Ocean-Surface NRCS at C-Band	5975
Vertical Air Motions and Raindrop Size Distributions Estimated Using Mean Doppler Velocity Difference From 3- and 35-GHz Vertically Pointing Radars	6048
Investigation of Azimuthal Variations From X-Band Medium-Grazing-Angle Sea Clutter	6110
Synthetic Aperture Radar	
Phase Estimation for Distributed Scatterers in InSAR Stacks Using Integer Least Squares Estimation	5671
Fast and Accurate Target Detection Based on Multiscale Saliency and Active Contour Model for High-Resolution SAR Images	5729
Wrapped Staring Spotlight SAR	5745
Coherent Change Detection Using InSAR Temporal Decorrelation Model: A Case Study for Volcanic Ash Detection	5765
Polarimetric Analysis of Compact-Polarimetry SAR Architectures for Sea Oil Slick Observation	5862
SAR Image Change Detection Based on Correlation Kernel and Multistage Extreme Learning Machine	5993
Single-Look SAR Tomography as an Add-On to PSI for Improved Deformation Analysis in Urban Areas	6119
SAR Raw Data Simulation for Ocean Scenes Using Inverse Omega-K Algorithm	6151
First Airborne Demonstration of Holographic SAR Tomography With Fully Polarimetric Multicircular Acquisitions at L-Band	6170
Spatial Resolution Improvement in GNSS-Based SAR Using Multistatic Acquisitions and Feature Extraction	6217

Global Navigation Satellite System			
Array-Aided Multifrequency GNSS Ionospheric Sensing: Estimability and Precision Analysis	A. Khodabandeh and P. J. G. Teunissen	5895	
A Statistical Model and Simulator for Ocean-Reflected GNSS Signals	J. L. Garrison	6007	
Satellite Systems			
Radiometric Characteristics of KOMPSAT-3 Multispectral Images Using the Spectra of Well-Known Surface Tarps	J.-M. Yeom, J. Hwang, C.-G. Jin, D.-H. Lee, and K.-S. Han	5914	
Suomi NPP VIIRS Solar Diffuser BRDF Degradation Factor at Short-Wave Infrared Band Wavelengths	N. Lei and X. Xiong	6212	

About the Cover: The cover illustrates radio-frequency interference (RFI) detected by the SMAP (Soil Moisture Active Passive) mission over East Asia and Japan. Values for the kurtosis statistic, which is used as an RFI detector in the SMAP L1B_TB ground processing algorithm, are shown, using either the fullband (upper plots) or subband (lower plots) datasets provided by SMAP. For more information please see “SMAP L-Band Microwave Radiometer: RFI Mitigation Prelaunch Analysis and First Year On-Orbit Observations,” by Mohammed *et al.*, which begins on page 6035.